The Development of SSM/I Rain-Rate Retrieval Algorithms Using Ground-Based Radar Measurements

RALPH R. FERRARO

NOAA/Satellite Research Laboratory, Camp Springs, Maryland

GERARD F. MARKS

S M Systems and Research Corporation, Bowie, Maryland

(Manuscript received 9 May 1994, in final form 3 January 1995)

ABSTRACT

Rainfall algorithms developed for the DMSP Special Sensor Microwave/Imager are presented and then "calibrated" against ground-based radar measurements to develop instantaneous rain-rate retrieval algorithms. These include both scattering- and emission-based algorithms. Radar data from Japan, the United States, and the United Kingdom have been used in the investigation. Because of the difficulties in accurately matching the satellite and radar measurements in both time and space, an approach where both measurements are grouped in 1 mm h^{-1} rain-rate bins provides a much more accurate set of measurements to be used in the derivation of coefficients for instantaneous rain-rate retrieval. Both linear and nonlinear relationships are developed, with the nonlinear fits being more accurate and supported by model simulations. An application of the derived instantaneous rain-rate relationships to an independent case is presented, with approximately a 10% error for the scattering algorithm when compared with radar-derived rain rates.

1. Introduction

The ability of satellite-borne passive microwave sensors to detect precipitation has been demonstrated by several investigators over the past decade. Instruments such as the *Nimbus-7* Scanning Multichannel Microwave Radiometer (SMMR) and most recently, the DMSP series of Special Sensor Microwave/Imagers (SSM/I) have been used to map regions of precipitation. Ongoing validation studies through international projects such as the Global Precipitation Climatology Project (GPCP), Algorithm Intercomparison Program (AIP), and the National Aeronautics and Space Administration (NASA) WetNet Project (Dodge and Goodman 1994) are confirming the ability of the SSM/I to generate rain fields reliably. Although there are several techniques available to identify areas of rain from these instruments, the conversion to an instantaneous rain rate is difficult because of the inhomogeneity of the rain field in the relatively large microwave footprints (i.e., "beam filling"). This problem is compounded by the scarcity of validation data, especially over the oceans. Additionally, the conversion to rain rate will have regional dependence based upon the physical processes of the precipitation regime. The derivation of coefficients for instantaneous rain-rate retrieval is based upon either empirical or theoretical methods. This investigation empirically derives rain-rate retrieval coefficients for SSM/I rain algorithms developed at the National Oceanic and Atmospheric Administration (NOAA) Satellite Research Laboratory.

The only ground measurements of rain that are available for the development of instantaneous rain-rate retrievals and their validation are from rain gauges and weather radar. Rain gauge data for hourly time periods are available over different parts of the world, but since they are point measurements, they do not give a representative measure of the rain in the large satellite field of view (FOV), unless they are of very high density. On the other hand, weather radar scan data are available on the order of every 10 min and are of high spatial resolution (e.g., on the order of 5-km resolution over 100 000 km^2). Although there are many documented sources of error in these measurements (i.e., Joss and Waldvogel 1990), particularly in the variability of Z–R relationships, radar does provide instantaneous rain measurements over a relatively large area, especially in regions where radar networks exist. Thus, in addition to the United States, countries such as Japan and those in western Europe operate radar networks that provide continuous ground coverage. Also, radar provides limited information about oceanic

Corresponding author address: Ralph R. Ferraro, NOAA/Satellite Research Laboratory, 5200 Auth Road, Rm. 712, Camp Springs, MD 20746.
E-mail: rferraro@orbit.nesdis.noaa.gov

rainfall in adjacent coastal waters. The fact that radar provides instantaneous observations of rain structure over large areas at high resolution makes it the best source of validation data for passive microwave satellite measurements. By treating the data with special care, these measurements can be used to develop coefficients for instantaneous rain-rate retrieval and will be demonstrated in the paper.

2. Previous studies

a. Rain algorithms

There are two methods of deriving rain rate from passive microwave observations: scattering and emission. These are discussed in more detail in section 4. Several investigators have developed instantaneous rain-rate retrieval algorithms using the scattering method. For the SSM/I, they include Adler et al. (1991), Spencer et al. (1989), and Grody (1991). Additionally, SSM/I emission algorithms are described by Petty (1990), Wentz (1990), and Grody and Ferraro (1992).

It should be noted that several emission algorithms have been developed and applied for use in climatological studies. While several investigators generate climate-scale products by averaging the instantaneous rain measurements over monthly timescales and larger spatial scales (e.g., 250 km), there is a class of algorithms that can only be used with monthly distributions of satellite measurements over large areas. Although it is not the intent of this paper to examine such algorithms, a few that warrant mentioning include Prabhakara et al. (1992), Wilheit et al. (1991), Berg and Chase (1992), and Weng (1992).

Finally, many of the satellite-based algorithms have been formulated from radiative transfer simulations. These deterministic approaches to rain-rate calculations are generally not practical to process large quantities of satellite data, especially on a routine basis. However, many investigators have used the simulations to determine the optimum set of channels to be used in the retrieval schemes. Studies on the sensitivity of the algorithms to other atmospheric variables (e.g., water vapor and cloud water) and surface roughness variables (e.g., wind speed) have led to the formulation of several of the above referenced algorithms. Some notable pioneers in the modeling aspects of microwave rain retrieval include Wilheit et al. (1977) and Wu and Weinman (1984).

b. Instantaneous rain-rate retrieval

Passive microwave satellite rain algorithms can be calibrated to retrieve instantaneous rain rates by using ground-based radar measurements that have been temporally and spatially matched with coincident satellite measurements. This approach was performed by several investigators, including Spencer (1986), Petty and Katsoras (1990, 1992), Alishouse et al. (1990), and Ferraro et al. (1992). In addition, the operational SSM/I rain-rate retrieval algorithm developed by SSM/I calibration and validation team was developed in this manner (Hollinger 1991).

Another approach is to use radiative transfer and cloud models to simulate a host of atmospheric and cloud profiles. The theoretical computations of brightness temperatures of these profiles can be applied to satellite measurements, which are then "inverted" to determine the rain rate. Model calculations of rain rate are typically validated and/or tuned to airborne in situ measurements of rain systems (e.g., Hakkarinen and Adler 1988), which provide high-resolution, multispectral observations of the rain system. Nonetheless, the use of theoretical brightness temperature to produce rain-rate relationships has been used successfully by investigators such as Kummerow and Weinman (1988).

3. Radar data and characteristics

Three sources of radar data were used in this investigation. Radar data from three different geographic areas for a wide range of weather systems were used to obtain as much variety as possible in SSM/I rain-rate relationships. Each radar dataset has its own set of characteristics and error sources. They are described below.

a. AMeDAS–radar composite

The Japanese Meteorological Agency (JMA) maintains a high-resolution network of rain gauges, supplemented by a weather radar network, which gives complete coverage of Japan and adjacent coastal waters. The rain gauge network is part of the Automated Meteorological Data Acquisition System (AMeDAS). The radar observation network consists of 20 land-based and 2 ship-based radars. The radar data are routinely digitized to a 500 km × 500 km grid, with individual grid boxes being 5 km. Hourly rainfall analyses are created from a composite of the AMeDAS automated rain gauge data and radars at 0.05° latitude by 0.0625° longitude resolution. A Z–R relationship of $Z = 200R^{1.6}$ (e.g., stratiform rainfall) is used for the radar data.

b. FRONTIERS

The U.K. Meteorological Office operates a network of weather radar data providing coverage over much of England, Wales, and Ireland. The FRONTIERS system presently consists of 14 radar installations. The radar scans at four elevation angles (up to 4°) with the scan sequence repeating every 5 min. A Z–R relationship of $Z = 200R^{1.6}$ is used to convert the measurements to rain rate. The data used in this investigation was compiled by the University of Bristol, who selected

matchups with SSM/I observations. The radar data was averaged to 15-km grid cells to coincide with the 85 GHz measurements.

c. *RADAP-II*

The RADAP-II data are compiled by the NWS Technique's Development Laboratory. It is stored in polar format of 2° azimuthal spacing by 1.85-km range bins from 20 to 230 km. The first 20 km of data are not archived due to ground clutter. The scans are taken every 10 min. The data are stored as digital video integrator and processor (DVIP) values and are integers from 0 to 15, which correspond to rainfall amounts increasing in intensity as DVIP increases. A complete scan consists of a sequence of tilts starting from the lowest tilt angle (0.5°) in 2° increments ending with the highest tilt (16°). The DVIP values are converted to dBZ by means of the a look-up table (Greene et al. 1983). There are on the order of a dozen stations included in the RADAP-II archive, located in the central and eastern United States. There is one coastal site as well that is located at Tampa, Florida. To convert the dBZ values to rain rate, the user can select upon a representative Z–R relationship. For this study, we chose a Z–R relationship developed by Austin (1987), $Z = 230R^{1.4}$, which represents a blend of convective and stratiform rain.

4. Characteristics of SSM/I data and algorithms

a. *SSM/I instrument*

The first SSM/I instrument was launched on 19 June 1987 aboard the DMSP block 5D-2 F-8 satellite. Other instruments have been launched into orbit aboard the F-10 (1 December 1990) and F-11 (28 November 1991) satellites. The SSM/I is a seven-channel radiometer measuring earth-emitted radiation at 19.35, 22.235, 37.0, and 85.5 GHz. All of the measurements are dual-polarization except at 22.235 GHz, where only vertical polarization is measured. For simplicity's sake, all of the subsequent referrals to the SSM/I channels will truncate the decimal (e.g., 85 GHz instead of 85.5 GHz) and will refer to the vertical and horizontal polarizations as V and H, respectively.

The DMSP satellites operate in a sun-synchronous orbit with an orbital period of about 101 min. The SSM/I instrument scans in a 102.4° segment of a circular rotation at an earth incidence angle of 53.1° that results in a swath width of approximately 1400 km. Sampling is every 25 km in both the scan direction and satellite direction for the 19-, 22-, and 37-GHz channels while 12.5-km sampling occurs for the 85-GHz channels. Table 1 summarizes some of the SSM/I instrument characteristics whereas more detail can be found in Hollinger et al. (1987).

For this study, data from the F-8 satellite has been used. Data in the commonly referred to format as "Wentz compact antenna temperature tapes" have been used for the F-8 (Wentz 1991). The 85V channel became increasingly noisy beginning in January 1988 and became unusable in May 1988. A stepwise linear regression scheme developed by the Hughes Aircraft Company to "synthesize" the 85V channel using the other six channels was used during periods beginning 1 May 1988. The appendix describes this routine and presents some error statistics on its performance.

TABLE 1. SSM/I instrument characteristics.

Frequency (GHz)	Polarization	Spatial resolution (km)
19.35	V, H	43 × 69
22.35	V	40 × 60
37.0	V, H	29 × 37
85.5	V, H	13 × 15

b. *SSM/I rain algorithms*

Both scattering- and emission-based rain algorithms will be used in this investigation. Because of the lack of sufficient validation data, especially over the ocean, the consensus as to which algorithm is the "best" has not yet been determined. The intercomparison programs supported by the GPCP and WetNet may eventually lead to a "consensus" rain algorithm, but it is the authors' feeling that the best SSM/I algorithm will be a blend of the best physical qualities of each of the approaches. The algorithms are briefly described herein.

1) SCATTERING ALGORITHM

In most precipitation systems, the rain layer extends above the freezing level, and as such, contains a mixture of water and ice particles. Depending upon the cloud microphysics and dynamical forcing (e.g., vertical velocities), the size and density of these ice particles will vary. The SSM/I measurements at frequencies of 37 and 85 GHz will be depressed by scattering if the ice particles increase in size to around 8 and 4 mm, respectively. Hence, the 85 GHz is more sensitive to the smaller ice particles. Grody (1991) developed a scattering index (SI), which is a measure of the temperature depression at 85 GHz due to the presence of ice. Care must be taken to remove other scattering media such as snow, sea-ice, and desert.

The scattering technique is best suited for land-based precipitation systems because the ice layer is typically thicker over land (Hakkarinen and Adler 1988). However, many large-scale oceanic systems contain ice as well, so that the scattering-based technique also works well for these cases. Possible problems occur in detecting rain events at high latitudes over the oceans, although very little validation data are available for

this region. Preliminary results from AIP-2 support this, as the emission-based algorithms generated more extensive regions of rain than the scattering algorithms. The motivation for using a scattering approach is to get global rain estimates over land and ocean. No other technique can be used to meet this objective.

The scattering index used in this study (Ferraro et al. 1994) is an improvement over the original one developed by Grody (1991). The main improvement is a stratified algorithm for land and ocean, with an enhanced sensitivity to oceanic scattering. Other improvements include better screening for anomalous scattering features such as frozen ground and unvegetated land. Additionally, the coefficients are derived for brightness temperatures, not antenna temperatures as was done in the original investigation. Specifically, the scattering index SI_{LW} is defined as

$$SI_{LW} = \begin{cases} SI_L = 451.9 - 0.44TB_{19V} - 1.775TB_{22V} \\ \quad + 0.00575TB_{22V}^2 - TB_{85V} \quad \text{(land)} \qquad (1a) \\ SI_W = -174.4 + 0.72TB_{19V} + 2.439TB_{22V} \\ \quad - 0.00504TB_{22V}^2 - TB_{85V} \quad \text{(water)}, \qquad (1b) \end{cases}$$

where TB denotes brightness temperature (K) and the subscript indicates the SSM/I channel. A value of SI greater than 10 K has been found to be a good global indicator of rain (Grody 1991). Lowering this threshold for regional applications will increase the area of rain and will include very light rain rates. However, this will introduce false rain signatures globally.

2) Emission algorithms

Over ocean, atmospheric liquid water Q can be retrieved using any of the SSM/I window channels. The frequencies at 19 and 37 GHz are best suited since they are the least sensitive to scattering, although 85 GHz can be used to retrieve Q as well (when scattering is not present) (Petty 1990; Weng and Grody 1994). At 19 or 37 GHz the variations in the brightness temperature are predominately due to clouds, water vapor, and rain. The smaller variations due to wind on the ocean surface is reduced by using vertical polarization measurements. Also, the contributions due to water vapor are removed using the 22-GHz channel (Grody and Ferraro 1992). Because the 37-GHz channel saturates at low rain rates and is influenced by ice scattering for some convective systems, the 19-GHz measurement of liquid water is best suited for all ranges expected over the global oceans. An algorithm to retrieve Q (kg m^{-2} or mm) at 19 GHz is

$$Q_{19} = -6.723[\ln(290 - TB_{19V}) - 2.850 - 0.405 \ln(290 - TB_{22V})]. \quad (2)$$

An empirical threshold is used to distinguish clouds from rain. By examining several global datasets, it was determined that rain is almost always present if $Q > 0.40$ mm. This value is comparable to that reported by Hinton et al. (1992) for rain in the Indian Ocean. Wentz (1990) found a much lower value of Q (0.18 mm) to be used as a rain/no-rain threshold for rain systems off the California coast, primarily in the winter season. This cutoff value included rain in the form of drizzle. For global applications, we feel that the higher value is representative of rain heavier than drizzle. However, the depth of the rain column (i.e., height of the freezing level) also influences the rain/no-rain threshold, and hence, has regional dependence.

5. Methodology and error sources

Cases of rain systems where coincident radar and SSM/I observations existed were identified and processed in the following manner. All of the radar observations within a 7.5-km radius of the SSM/I FOV center were averaged. This is effectively averaging the radar data to the 85-GHz FOV. For the AMeDAS and FRONTIERS radar data, the rain rates already supplied were simply linearly averaged. For the RADAP-II set, the dBZ values were converted to rain rate, then linearly averaged to produce a mean rain-rate value.

a. Error sources

In doing a study of this type, there are several sources of error that occur. There are errors in the SSM/I measurements, rain retrieval algorithms, and radar data. Some of these are discussed below.

1) SSM/I errors

There are two primary classes of errors in the SSM/I rain retrievals: instrument errors and precipitation algorithm errors. Aside from the increased noise problem experienced by the 85-GHz channels during the first year of SSM/I operation, the SSM/I instruments have been very stable sensors. Some minor adjustments to the measurements can be applied to account for variations at different beam positions (see Wentz 1991), as well as gain variations (Hollinger 1991). Fortunately, the SSM/I data does not suffer from pronounced nonlinear instrument variations common to visible and IR sensors. Unfortunately, the SSM/I does suffer from navigation errors, reportedly on the order of 25 km. However, postlaunch corrections have been made (Hollinger 1991; Wentz 1991) that reduce the navigation error to less than 10 km. These errors are still large enough to cause errors in matching with coincident radar data, which is at a resolution of 5 km or less. A final source of instrument error comes from the synthetic 85V measurements. As discussed in the appendix, errors on the order of 2 K are evident from the 85V synthesis.

The second class of error comes from the SSM/I algorithms. Because the FOV size can be rather large compared to the rain cell size, especially in the cases of small convective cells, the rain signal may not be strong enough to be detected by the instrument. This is a function of the channels selected in the algorithm. Additionally, this beam-filling problem is compounded by the nonlinearity of the brightness temperature–rain-rate relationships, which is also a function of frequency (i.e., see Wu and Weinman 1984). Another problem occurs with shallow convective and weak stratiform rain systems. The scattering-based algorithms, which rely on the presence of ice particles to detect rain, do not perform well with these so-called "warm rain" systems since little or no ice is present. The emission-based oceanic algorithms, relying only on the presence of water droplets, generally perform better with detecting rain in these systems (e.g., Adler and Hakkarinen 1991). Over land, orographically induced rain, having similar characteristics to shallow convective rain, is generally not detected by the SSM/I or is detected as very light rain.

2) RADAR ERRORS

An underlying assumption for investigations of this type is that the radar data is the "truth," and hence, the SSM/I retrievals should be anchored to the radar-derived rain values. This, however, is an inaccurate assumption since there are several documented sources of error in radar-derived rain rates. Petty and Katsoras (1992) reported on these types of errors and how to minimize them in a comparison with *Nimbus-7* SMMR rain measurements. It is, however, important to mention some of the sources of error. These include radar beam filling, ground clutter, bright band and other "false" signatures, radar calibration, and Z–R relationship variability with storm type (i.e., see Alishouse et al. 1990, Fig. 2).

3) MATCHUP ERRORS

A final source of error is collocation of the ground-based radar measurements with the satellite observations. This includes both time and space mislocations, which make accurate matchups between the two extremely difficult. Time differences in the radar and satellite measurements result in errors due to the movement of the rain systems as well as changes in the rain cells themselves. If both data sources are gridded to the same projection, one generally sees similar spatial structures between the SSM/I and radar rain fields. However, there is generally a displacement or "shift" in rain fields if the two data are superimposed. This can be attributed to differences in observation time and geolocation errors. Compounding these basic sources of error is the fact that the radar is viewing "up" at the rain field while the satellite is viewing "down" at an oblique angle. This also makes accurate matches between the radar and satellite difficult. However, as is described herein, special treatment of the data can help to minimize these sources of error.

b. Quality control

Despite all of these error sources, valid results can be obtained if special care is taken when performing the data matchups. The following rules were generally followed when preparing the SSM/I and radar database:

1) Use only data which are within 10 min of each other. This minimizes problems due to changes in storm intensity and structure.
2) Use only data within 150 km of radar center. This minimizes the effect of radar beam filling.
3) For ocean data, stay at least 50 km from land. This minimizes the effect of land contamination, especially due to the SSM/I geolocation errors. Additionally, this reduces the effects due to partial beam filling of the SSM/I 19-GHz FOV by land.
4) Use only data where SSM/I generally indicates rain. This minimizes the effects due to radar ground clutter, bright band, etc.

6. Results

For each of the radar datasets, matches between rain events and SSM/I orbits were made. As was previously discussed, the radar data were spatially averaged to the 85-GHz FOV to produce a field of rain rates. The SSM/I and radar data, now effectively gridded to the same field, were then "matched" through an interactive computer system. Table 2 summarizes the datasets compiled for each radar location. The largest dataset was from Japan (nearly 8700 individual matchups between 15-km average radar and SSM/I FOV), followed by the RADAP-II (5400 matchups), and the FRONTIERS (2300 matchups). The Japan dataset contains data from spring and summer, while the RADAP-II and FRONTIERS data contain data from summer and fall. Overall, a fairly wide variety of rain systems are contained in the data.

a. Scatterplots

The initial analysis performed was a least-squares fit between the SSM/I rain predictors and the radar rain

TABLE 2. Summary of the SSM/I and radar matchup datasets as a function of radar location.

		Number of observations		
Radar type	Dates	Land	Ocean	Total
AMeDAS	June–August 1989	2046	6635	8681
RADAP-II	July–November 1987	4835	532	5367
FRONTIERS	July–October 1987	1535	742	2277

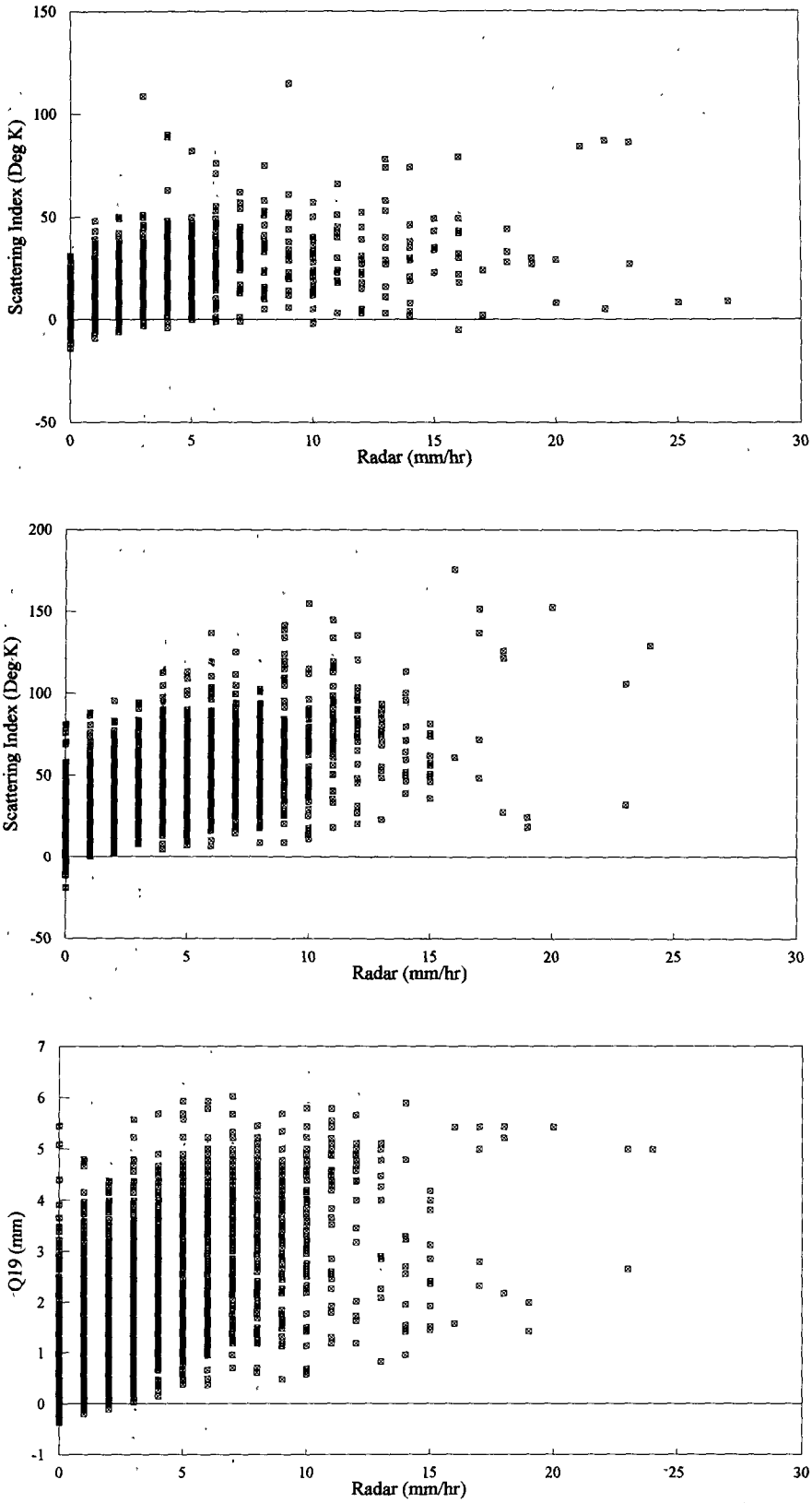

FIG. 1. SSM/I scattering index values (K) for (a) land, (b) ocean, and (c) cloud liquid water (mm) as a function of radar rain rate for the AMeDAS dataset.

rates. Figure 1 shows the scatterplots for the SI_{LW} and Q_{19} as a function of rain rate for the Japan dataset. The data are separated for land and ocean data. The correlation coefficients for both linear and nonlinear fits are given in Table 3. The Japan dataset was chosen for display since it contained the largest number of data observations. The results were somewhat disappointing, but yet, not surprising given the many sources of error previously described. Despite the tremendous scatter in the data, there is an increase in rain rate with increasing SI and Q, which is the relationship we expected. Similar type results were found with data from the other radar sites, although the degree of scatter varied with radar site and algorithm. These are also presented in Table 3. The AMeDAS data undergo the highest level of quality control out of the three radar datasets used, and this is confirmed by our analysis by having the highest overall correlations.

TABLE 3. Summary of correlation coefficients for both linear and nonlinear fits as a function of radar site, land and ocean, for each of the algorithms using all of the data observations.

Radar	Regression fit	SI_L	SI_W	Q_{19}
AMeDAS	Linear	0.54	0.65	0.55
	Nonlinear	0.47	0.32	0.23
RADAP-II	Linear	0.28	0.46	0.53
	Nonlinear	0.10	0.38	0.43
FRONTIERS	Linear	0.30	0.43	0.34
	Nonlinear	0.30	0.44	0.38

b. Binned analysis

The regression of the individual point data does not meet our original objective since it does not place equal emphasis on the entire range of rain rates. The least-squares fit actually places emphasis on the lightest rain rates since this is where most of the data occurs. However, it will yield the largest errors for heavy, but less frequent rain rates. In order to properly develop relationships between SSM/I predictors and rain rate, radar data should be used to develop representative SSM/I predictors over a wide range of rain rates. This is analogous to radiative transfer models calculations, which compute TBs emitted from a variety of atmospheric conditions to simulate the TB–rain-rate relationships (e.g., Wu and Weinman 1984), irregardless of the frequency distribution of the rain rates. However, an added advantage of the empirical approach is that the SSM/I sensor properties (i.e., antenna pattern, varying FOV size with frequency, etc.) are automatically included in the satellite–radar matchups.

To better pursue this objective, the radar data were binned in 1 mm h^{-1} rain rates, and the SSM/I measurements in these bins were averaged. The result of this analysis is illustrated in Fig. 2, which shows the average SI and Q values as a function of the 1 mm h^{-1} rain bins for 0–15 mm h^{-1}. In addition, Table 4 shows the number of observations, mean SI and Q values, and standard deviation (SD) as a function of radar site. The most obvious improvements from the original analysis is the much more expected trends in the data, as well as the smoothness in the SSM/I rain-rate relationship.

1) OVER LAND

Over land, there is an obvious increase in SSM/I SI with rain rate up to about 10 mm h^{-1}. The results from the Japan and U.K. radar sites are in close agreement, with the U.S. radar data indicating a higher SI value at each rain rate. Beyond 10 mm h^{-1}, the data tends to saturate and trends become confused. Examining the number of observations in each rain bin, it becomes evident that the results at the higher rain rates become less reliable when the number of observations falls below 20. It should be noted that higher rain-rate values have been excluded from the analysis because of an even more reduced data sampling. Nonetheless, the results indicate a nonlinear relationship between SSM/I, SI, and rain rate over land. Other features of interest include the fairly stable SD values with rain rate (i.e., about 15 K) and the rain/no-rain threshold of about 10 K, which confirms those results originally found by Grody (1991).

2) OVER OCEAN

Over ocean, similar good results were found, with an even smoother fit evident up to about 12 mm h^{-1} for both the SI and Q. This is particularly true with the AMeDAS data, which had the largest amount of data available. The RADAP-II data are very noisy, and this is due to the small sample size, data from only one radar (e.g., Tampa, Florida), and the poorer quality control of the RADAP-II data. As was the case for land, the results deteriorate when the sample size drops below 20. In addition, nonlinear relationships are apparent for both the SI and Q. Also, there again is a fairly stable SD value with rain rate (except for the RADAP-II).

3) DISCUSSION

The binned approach to the SSM/I and radar matchups clearly fulfills our requirement for the development of instantaneous rain-rate coefficients for the SSM/I algorithms. Namely, it has produced a dataset of representative SSM/I predictors over a wide range of rain rates. It is interesting to understand why this method works. In section 5, the wide variety of error sources in the SSM/I, radar, and matchup procedure are discussed. Clearly, the binning approach minimizes, to some extent, the time–space mismatches between the SSM/I and radar. This effectively accounts

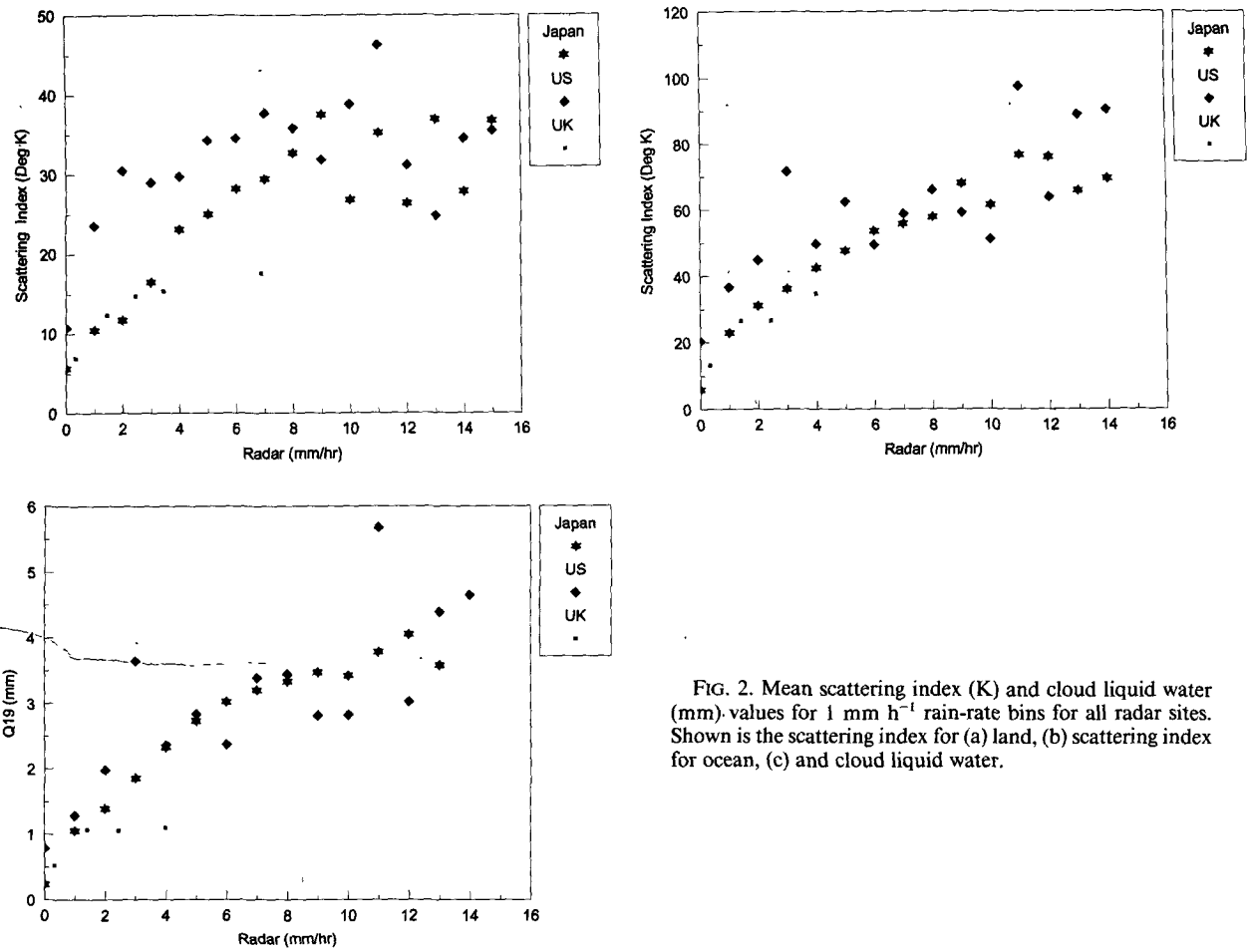

FIG. 2. Mean scattering index (K) and cloud liquid water (mm) values for 1 mm h^{-1} rain-rate bins for all radar sites. Shown is the scattering index for (a) land, (b) scattering index for ocean, (c) and cloud liquid water.

for the possible displacement by a pixel or two, of the SSM/I and radar observation of the same rain cell within an entire rain system. Additionally, the binning approach characterizes the "climatological" SSM/I rain-rate relationships. Clearly, these relationships are region and season dependent, as is evident in the differences found between the various radar sites in this investigation. Hence, the errors associated with applying these relationships for global rain-rate retrievals will vary with rainfall regime.

It should be noted, however, that the data could also be binned by SI or Q value, with a mean radar rain rate calculated for each bin. Because of the larger dynamic range in data values for the SSM/I parameters (e.g., 0–150 K for the SI versus 0–25 mm h^{-1} for the radar), the binned values will vary according to the size of the bin chosen. Furthermore, the results can be different from those obtained by binning the data by radar value, as was done in this study. However, since the radar values were generally in discrete 1 mm h^{-1} categories, it was a logical grouping for the SSM/I values. Additionally, this binning method provided a large dynamic range in rain rate that was needed to obtain representative values of SSM/I parameters as a function of rain rate.

c. *Rain-rate retrieval equations*

The binned approach has allowed for the generation of representative SSM/I predictors as a function of rain rate for both land and ocean. This dataset can be used to develop rain-rate retrieval equations, which will now assign equal weight to the data at each rain rate, unlike the original dataset of individual matchups that is biased toward the more frequent, lower rain rates. Least-square fits were developed for each radar site individually, as well as for the combined dataset. Because the stability of the binned datasets deteriorated at the higher rain rates due to the smaller sample sizes (and also varied for each radar site), regression fits were made with subjective removal of "outlier" data points. The results of the best linear and nonlinear fits to the data are summarized in Tables 5 and 6. The nonlinear fits that performed the best were in the form of a power fit for the SI algorithms (e.g., $R = a\mathrm{SI}^b$) and an exponential for the Q [e.g., $R = a \exp(bQ_{19})$]. As will

TABLE 4. Summary of the number of observations, mean, and standard deviation of SSM/I predictors for rain-rate bins 0–15 mm h^{-1} for (a) AMeDAS, (b) RADAP-II, and (c) FRONTIERS.

Rain bin (mm h^{-1})	Num. obs. land	SI_L mean	SI_L SD	Num. obs. ocean	SI_W mean	SI_W SD	Q_{19} mean	Q_{19} SD
(a) AMeDAS								
0	393	4.1	7.6	1736	5.9	10.7	0.2	0.6
1	440	8.9	8.8	1757	23.0	13.0	1.1	0.7
2	454	11.1	9.1	957	31.2	13.0	1.4	0.9
3	259	16.1	12.0	683	36.2	12.8	1.9	1.0
4	129	22.7	15.2	392	42.6	16.2	2.3	1.1
5	102	22.9	14.3	252	47.7	18.8	2.7	1.2
6	68	27.4	15.4	233	53.8	20.7	3.0	1.2
7	36	29.4	13.9	191	55.8	20.3	3.2	1.0
8	27	32.8	16.9	122	57.9	21.2	3.3	1.1
9	16	35.6	24.6	102	68.1	26.0	3.5	1.1
10	26	25.8	13.8	67	61.5	26.4	3.4	1.2
11	13	32.9	16.3	44	76.7	27.2	3.8	1.2
12	15	26.3	17.2	25	76.0	27.4	4.1	1.2
13	12	36.9	22.1	14	65.9	21.7	3.6	1.3
14	10	27.8	19.9	14	69.5	20.3	2.8	1.3
15	4	36.8	8.8	12	55.6	13.8	2.8	0.8
(b) RADAP-II								
0	3289	10.7	13.2	264	20.5	20.7	0.8	0.9
1	602	23.5	16.1	48	36.7	31.1	1.3	1.4
2	248	30.5	15.7	44	44.9	33.2	1.9	1.7
3	158	29.0	14.1	19	71.7	40.9	3.6	2.1
4	96	29.7	16.5	16	49.8	31.2	2.4	1.8
5	91	34.2	15.6	10	62.5	35.0	2.8	2.1
6	56	34.5	18.4	10	49.6	39.6	2.4	2.1
7	51	37.7	11.4	10	58.8	40.6	3.4	2.6
8	39	35.8	15.8	7	66.0	35.6	3.4	2.2
9	29	31.8	16.1	10	59.3	41.3	2.8	2.3
10	30	38.8	20.0	6	51.1	32.7	2.8	2.2
11	16	46.3	19.9	7	97.6	16.9	5.7	0.9
12	19	31.2	14.8	4	63.8	44.1	3.0	2.6
13	7	24.8	16.1	1	89.0	—	4.4	—
14	14	34.5	15.4	5	90.5	30.0	4.7	1.7
15	13	35.5	19.0	4	69.4	34.3	3.8	2.4
(c) FRONTIERS								
0	1257	6.9	7.2	634	13.2	11.3	0.5	0.3
1	171	12.3	9.6	63	26.6	18.9	1.0	0.2
2	53	14.7	10.5	23	26.7	14.4	1.1	0.2
3	25	15.3	7.9	23	34.8	15.6	1.1	0.2
4	0	—	—	0	—	—	—	—
5	0	—	—	0	—	—	—	—
6	29	17.5	16.1	0	—	—	—	—

be discussed shortly, both these nonlinear fits have physical significance and will produce more realistic rain fields than linear rain relationships.

In general, the nonlinear fits outperformed the linear fits. This was especially true for the higher quality datasets from Japan and the United Kingdom. The correlations all exceeded 0.8 over land and ocean, except for the RADAP-II ocean dataset, which was from one radar site and contained the fewest data observations. The differences in the regression coefficients are in part, due to the different rainfall characteristics of each region. Shown in Fig. 3 is a comparison of the predicted SSM/I rain rates as a function of SI and Q for each of the radar sites, as well as the combined relationships. The x and y axes have been interchanged in this figure since the SSM/I parameter is now the independent variable, while rain rate is dependent.

Over land, the RADAP-II relationship will produce the least amount of rain for the same SI value. This is attributed to the predominance of strong convective rain systems in the dataset. The U.K. equation will produce the most rain at a given SI value. However, this relationship is clearly limited since the input data

TABLE 5. Summary of the correlation coefficients as a function of radar site, land and ocean, for each of the algorithms using the binned datasets. The linear regression is in the form $R = a\text{SSMI} + b$, where SSMI represents both the SI and Q_{19}, while the nonlinear is in the form $R = a\text{SI}^b$ for the scattering index, $R = a\exp(bQ_{19})$ for the cloud liquid water algorithm.

Radar	Regression fit	SI_L	SI_W	Q_{19}
AMeDAS	Linear	0.85	0.96	0.86
	Nonlinear	0.94	0.99	0.93
RADAP-II	Linear	0.80	0.78	0.77
	Nonlinear	0.81	0.73	0.71
FRONTIERS	Linear	0.86	0.93	0.76
	Nonlinear	0.98	0.98	0.93
Combined	Linear	0.81	0.86	0.86
	Nonlinear	0.82	0.90	0.84

values did not exceed 6 mm h^{-1}. It is evident that large ice is very rare in U.K. rain systems. The combined relationship appears to be weighted toward the AMeDAS at the low rain rates, and the RADAP-II at the high rain rates.

It is interesting to note that the use of the power fit creates a relationship that is analogous to the radar Z–R relationship. Here, the SSM/I SI acts as a reflectivity parameter. The power fit produces lower rain rates at low to moderate rates than a linear fit (not shown), and then higher rain rates than a linear fit for rain rates in excess of 15 mm h^{-1}. However, because of the tendency of the relationship to accelerate toward high rain-rate values for extreme scattering cases, it is advisable to set a maximum allowable rain rate. A value of 30 or 35 mm h^{-1} appears to be a reasonable value for a 15-km-averaged rain rate.

Over ocean, we again see similar results to that over land for the SI. Because of rainfall microphysics (e.g., less vertical motion/less large ice), the rainfall over the United Kingdom tends to be heavier for the same SI value than that over Japan and the United States. In addition, the relationship for the United States produces less rain for the same SI value than for the United Kingdom and Japan, and again, this is most likely due to the prevalence of larger ice in the U.S. dataset. Examining the curves for the emission algorithm, the relationships from Japan and the United States are extremely similar up to about 3 mm, then depart beyond that. Again, the values over the United Kingdom are much different, and this can be attributed to the low range of rain rates used to produce this relationship, as well as the lower amounts of Q attainable in the higher latitudes.

d. Comparison of results to model simulations

Because of the empirical nature of this investigation, it is important to examine the robustness of the binned data by making comparisons to radiative transfer simulations. Shown in Figs. 4 and 5 are plots of the mean TBs for the vertically polarized SSM/I measurements as a function of rain rate using the combined binned dataset. Individual plots are provided for land (Fig. 4) and ocean (Fig. 5), and for 19 GHz (Figs. 4a and 5a), 37 GHz (Figs. 4b and 5b), and 85 GHz (Figs. 4c and 5c). Also shown in Figs. 4 and 5 is data representing the model results obtained by Bauer and Schluessel (1993). The fit to the model was generated by averaging the simulated values generated for a variety of surface and atmospheric situations, and are denoted by the boxes at 5 mm h^{-1}. Also indicated are the range of TBs for the simulations, denoted by the shaded region. These are shown to represent the full range of "possible" TBs given the various initial conditions used in the model simulations.

1) OVER LAND

Over land, the 19-GHz TB shows virtually no response to increasing rain rate. Differences are evident at each rain rate as a function of radar location, and this is primarily due to variations in surface temperature. Note how the U.K. data is colder than that over Japan and the United States. The mean model results exhibit a small decrease in TB with rain rate [approximately 1° $(\text{mm h}^{-1})^{-1}$] in response to volume scattering by ice particles. This feature is not evident in the actual SSM/I measurements and can be explained by the large footprint sizes at this frequency (see Table 1). This beam filling in combination with the long wavelengths makes the scattering signal at 19 GHz nearly impossible to detect with the SSM/I.

The 37-GHz data show a slight decrease in TB with increasing rain rate, with effects of surface temperature

TABLE 6. Summary of regression coefficients using binned data. The nonlinear fit is for a power fit for the SI and an exponential fit for Q_{19}.

Radar	Regression	SI_L	SI_W	Q_{19}
AMeDAS	Linear	$a = 0.426$	$a = 0.154$	$a = 0.0348$
		$b = -2.83$	$b = -2.04$	$b = -2.36$
	Nonlinear	$a = 0.0257$	$a = 0.0012$	$a = 0.6227$
		$b = 1.734$	$b = 2.168$	$b = 0.800$
RADAP-II	Linear	$a = 0.217$	$a = 0.169$	$a = 0.027$
		$b = -2.09$	$b = -3.30$	$b = -1.33$
	Nonlinear	$a = 0.0051$	$a = 0.0015$	$a = 1.31$
		$b = 1.947$	$b = 2.022$	$b = 0.480$
FRONTIERS	Linear	$a = 0.531$	$a = 0.162$	$a = 0.0427$
		$b = -4.18$	$b = -2.06$	$b = -1.97$
	Nonlinear	$a = 0.0008$	$a = 0.0005$	$a = 0.0480$
		$b = 3.051$	$b = 2.544$	$b = 3.634$
Combined	Linear	$a = 0.258$	$a = 1.732$	$a = 0.029$
		$b = -1.45$	$b = -2.67$	$b = -1.38$
	Nonlinear	$a = 0.036$	$a = 0.0032$	$a = 0.805$
		$b = 1.491$	$b = 1.873$	$b = 0.630$

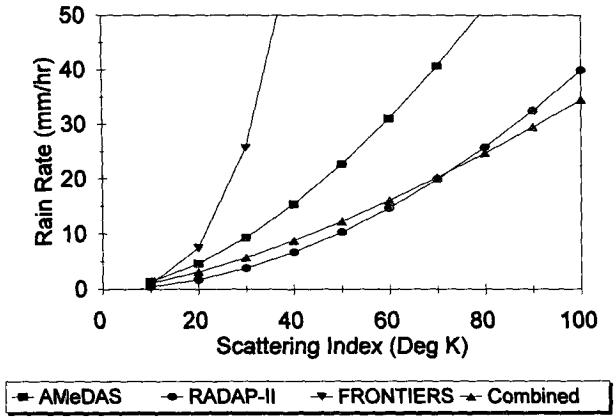

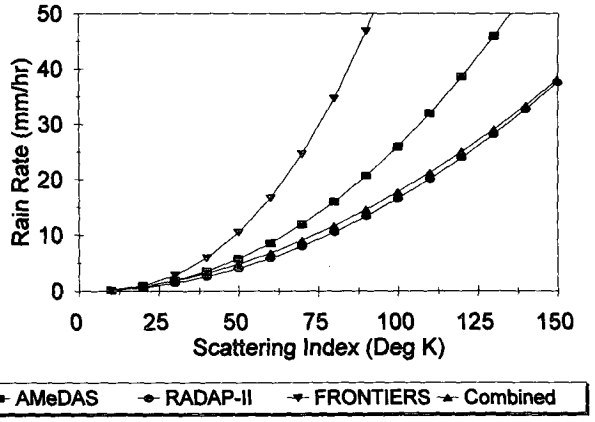

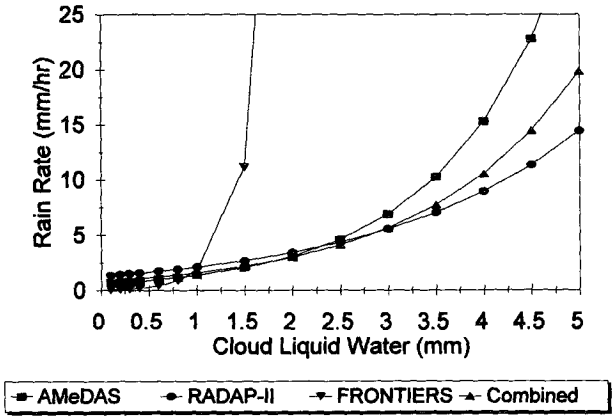

FIG. 3. Comparison of retrieved rain rate for (a) land and (b) ocean using scattering index algorithms, and (c) ocean emission, fit using binned data.

still evident. The mean model results show a moderate decrease in TB with rain rate [approximately 1.5° $(\text{mm h}^{-1})^{-1}$]. Again, the effects of scattering are reduced by beam filling, except in the case of extreme convective storms, a few of which were present in the RADAP-II dataset.

At 85 GHz, the decrease in TB with rain rate is now evident in both the model data and SSM/I measurements. Both data show a large decrease in TB with rain rate [approximately 2° $(\text{mm h}^{-1})^{-1}$]. For the SSM/I, the detectability of this feature is due to both the shorter wavelengths being more sensitive to the ice signature, as well as the higher spatial resolution. Differences from the "average" model conditions to those obtained with the SSM/I and radar data can be partially explained by the variety of initial conditions used in the model simulations.

In summary, the dataset produced by the "binned" method agrees reasonably well with model simulations. The largest differences appear to be explained by partial beam filling the SSM/I footprints at 19 GHz, and to a lesser degree, at 37 GHz. More importantly, the results agree surprisingly well at 85 GHz, which is the channel possessing the highest spatial resolution and the greatest sensitivity to ice scattering. It should be noted that the modeling of surface effects, conditions, and their variability, as well as the scattering effects due to ice, is extremely difficult and, hence, places much uncertainty in any model results.

2) OVER OCEAN

At 19 GHz, both the SSM/I observations and the model exhibit nearly the same rate of change in TB with rain rate [approximately 3° $(\text{mm h}^{-1})^{-1}$]. This is in response to the greater absorption and emission by rain drops. Lower TBs are found with the U.K. radar data, which can be explained by "colder" background conditions (e.g., sea surface temperature and drier atmosphere). The RADAP-II data (from Tampa, Florida) exhibit more scatter than those from the other two radar sites, and this is due to the greater degree of false radar signatures in the measurements.

At 37 GHz, both the SSM/I and model show an increase in TB with rain rate but show a saturation at around 6 and 10 mm h^{-1}, respectively. This is caused by increased sensitivity to rain drops at this frequency, as well as the effects of scattering due to rain and ice at higher rain rates. The differences between the saturation rain rate can be attributed to beam filling in the SSM/I.

Finally, at 85 GHz, the agreement between the simulations and the SSM/I data is not as good as was seen

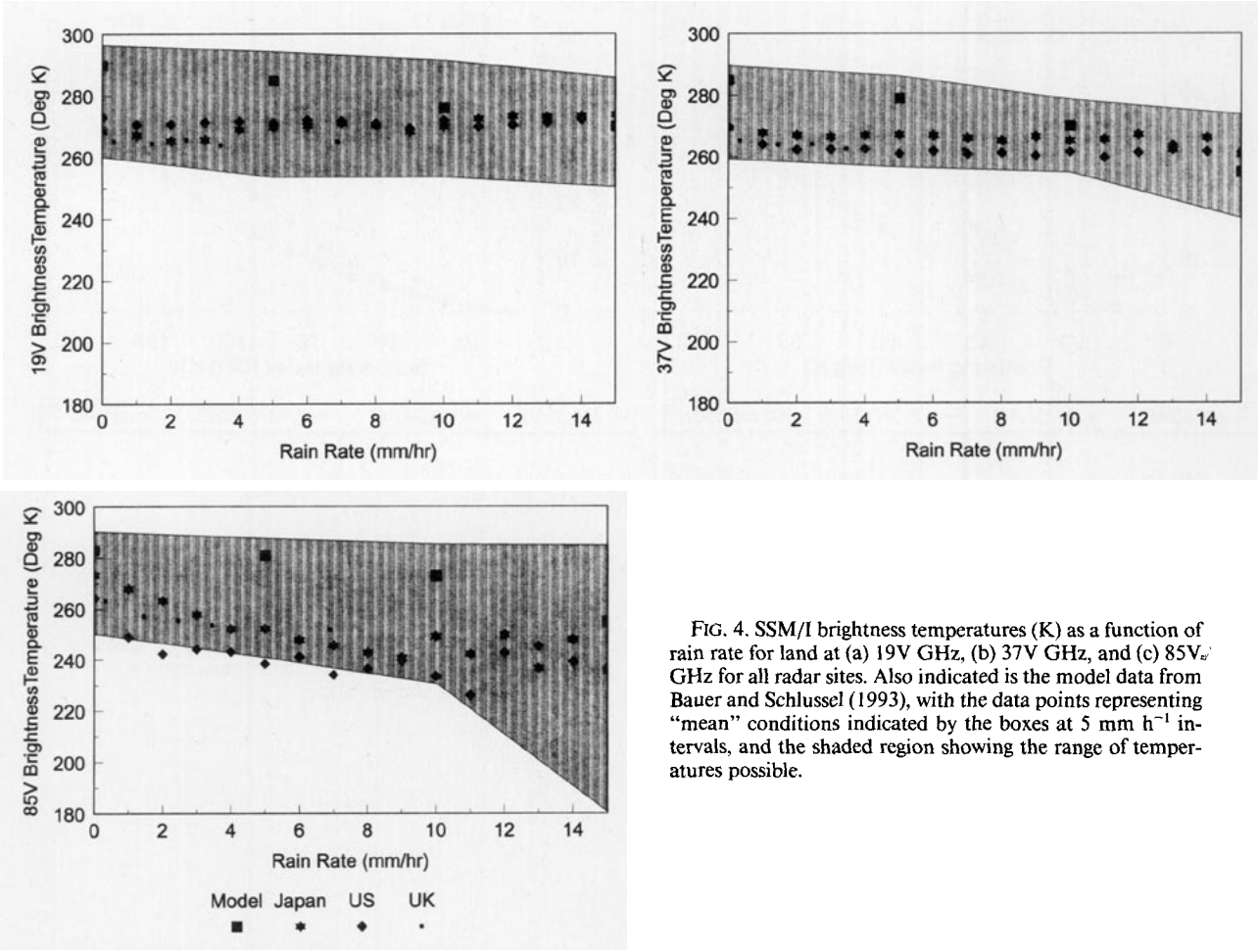

FIG. 4. SSM/I brightness temperatures (K) as a function of rain rate for land at (a) 19V GHz, (b) 37V GHz, and (c) 85V GHz for all radar sites. Also indicated is the model data from Bauer and Schlussel (1993), with the data points representing "mean" conditions indicated by the boxes at 5 mm h^{-1} intervals, and the shaded region showing the range of temperatures possible.

at 19 and 37 GHz. However, both datasets indicate a decrease in TB with increasing rain rate due to volume scattering by ice and raindrops. The SSM/I data actually shows a greater rate of TB decrease than the model results. The large differences between the magnitudes of the TB values can be attributed to assumptions about ice content in the model simulations.

Over ocean, the SSM/I and model simulations agree reasonably well. The agreement is somewhat better than that over land (especially at 19 and 37 GHz), which is due to the easier aspect of modeling ocean surface effects than those over land. The important features to note are the TB increases with rain rate at 19 and 37 GHz, with a saturation effect at moderate rain rates at 37 GHz. The 85-GHz data show a decrease in TB with rain rate.

7. Application of equations to individual case

To test the performance of the algorithms, a swath of SSM/I measurements not used in the assembled matchup database was selected, and SSM/I rain rates were derived and compared with the radar. An interesting case of rainfall over Japan and adjacent coastal water occurred at 2013 UTC 13 August 1989. Shown in Fig. 6 is the AMeDAS radar data (left), and SSM/I derived rain rates using the SI (center) and the Q_{19} (right). The SSM/I rain rates were generated using the nonlinear relationships from the combined datasets. The Q_{19} retrievals are made over ocean only and contain some contamination due to land in the FOV near coastlines. Also, the radar data are not available over the entire SSM/I swath, denoted by the lightest gray shade.

The radar indicates a band of rain stretching from the northernmost island southwestward across the main island, and then paralleling the north coast. Rain rates in this band exceed 16 mm h^{-1}. Another area of lighter rain showers is indicated offshore south of Japan. The SSM/I retrieved rain rates from both algorithms agree qualitatively with the radar, with the rain area, and with regions of maximum rain generally in the same area. Maximum rain rates with the scattering algorithm are approximately 12 mm h^{-1}, while those from the emission algorithm are over 16 mm h^{-1}.

Collecting the data over land and ocean for most of the rain areas reveals that the mean rain rate for the radar was 4.3 mm h^{-1} over land and 2.3 mm h^{-1} over

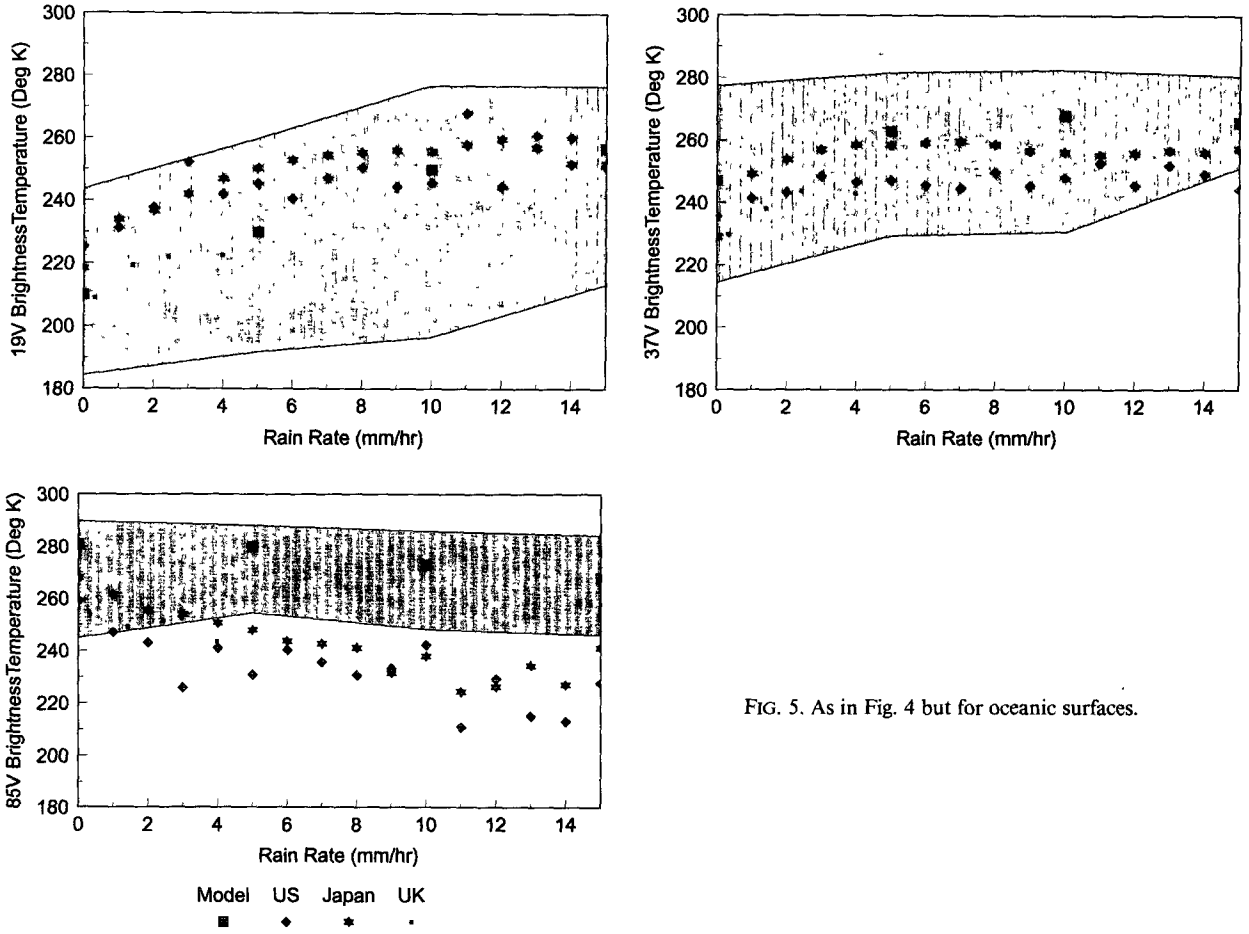

FIG. 5. As in Fig. 4 but for oceanic surfaces.

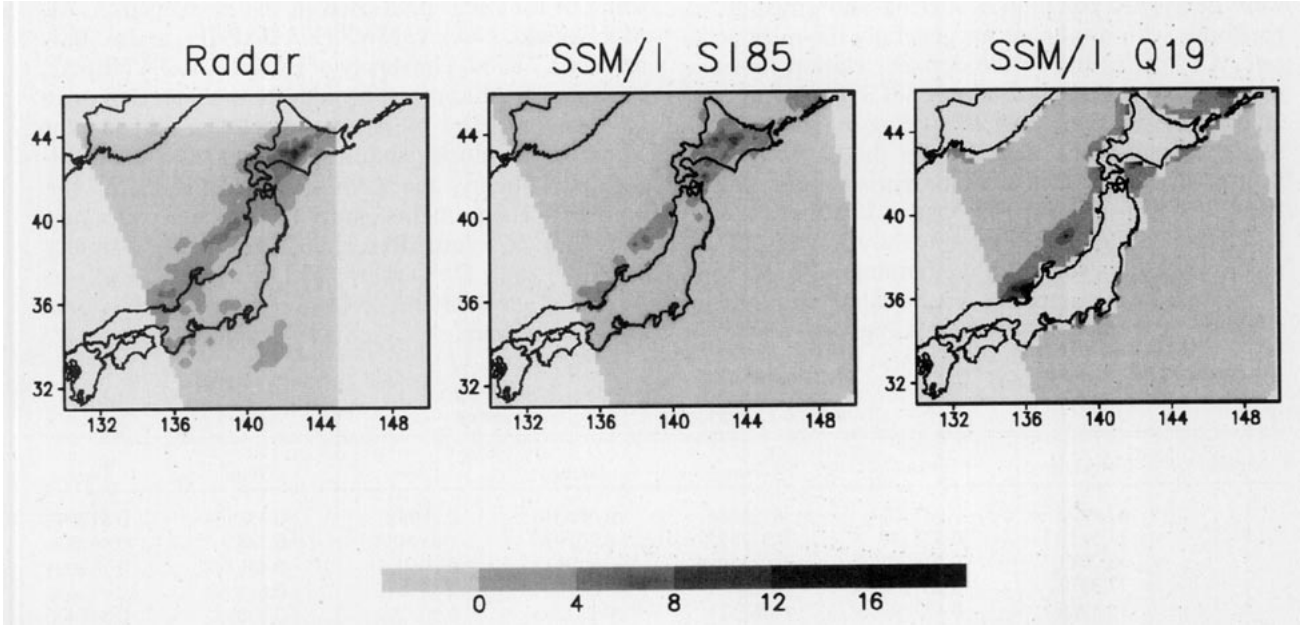

FIG. 6. Radar rain rate (left), SSM/I SI derived rain rate (center), and SSM/I Q_{19} derived rain rate (right) for 2013 UTC 13 August 1989. Units are millimeters per hour. The SSM/I swath region is denoted by the lightest gray shade.

ocean. The mean rain rate for the scattering algorithm was 4.0 and 2.1 mm h^{-1}, respectively, for land and ocean. This amounts to approximately a 10% error in retrieved rain rate, if the radar data is assumed to be correct. The Q_{19} algorithm produces a mean rain rate of 2.8 mm h^{-1}, which amounts to approximately a 20% error.

8. Summary and conclusions

In this investigation, high-quality ground radar measurements were used to develop coefficients to be used with SSM/I rainfall algorithms to retrieve instantaneous rain rates. A coincident radar and SSM/I dataset of nearly 17 000 observations was assembled from radar sites in the United States, Japan, and the United Kingdom. Tremendous scatter occurred when plots of the entire ensemble of data were made. This can be attributed to the varying atmospheric characteristics of the data obtained, as well as the difficulties in obtaining accurate time and space matchups between ground-based measurements and satellite observations. The standard least-squares fit to the data was found to be inadequate to produce usable retrieval coefficients because of the data scatter. Additionally, because the majority of the rain in the data was at the lower rain rates, this approach does not provide a representative range of rain rates needed for proper SSM/I rain-rate retrieval algorithms. A binning technique, where both the SSM/I and radar data are grouped into 1 mm h^{-1} bins, provides a much more useful dataset that minimizes both of these problems. The robustness of this approach was confirmed by comparing the mean brightness temperatures for each "bin" to the model simulations of Bauer and Schluessel (1993). Rain-rate retrieval equations were developed for both scattering and emission algorithms, with nonlinear fits generally the most accurate. An application of the derived relationships was presented on an individual swath of SSM/I data, with an error of approximately 10% being obtained for the scattering algorithm, and 20% for the emission algorithm. The continuing intercomparison programs of the GPCP and WetNet will offer independent validation data that will help determine the accuracy of these relationships to a variety of meteorological conditions.

With the development of better quality radar systems such as the United States Next Generation Weather Radar (NEXRAD) and those used to support the NASA Tropical Rainfall Measuring Mission (TRMM), more accurate retrieval coefficients may be possible. However, the regional dependence of the SSM/I rain-rate relationships (i.e., precipitation physical process) and the nonuniqueness in Z–R relationships will still be major difficulties to overcome. Additionally, unless the errors associated with matching satellite- and ground-based radar can be reduced, the improved radar measurements may not yield much better results. What is more important for our work is to obtain data from a wide range of rain systems, particularly over the oceans, to investigate the variability in the rain-rate relationships.

TABLE A1. Categories and rms errors for stratified SSM/I dataset.

Category	19H–85H class	85H class	rms error
1	19H–85H < −70	All data	1.6 K
2	−70 < 19H–85H < −50	85H < 210	2.7
3	−70 < 19H–85H < −50	85H > 210 K	3.4
4	−50 < 19H–85H < 0	85H > 180 K	2.5
5	−50 < 19H–85H < 0	85H < 180 K	2.7
6	0 < 19H–85H < 30	All data	2.4
7	30 < 19H–85H	All data	2.3

Acknowledgments. The authors express sincere gratitude to Dr. Norman Grody (NOAA) for his guidance and support on the project, as well as the opportunity to publish the results. Also, we thank Dr. Peter Bauer (German Aerospace Research Establishment) for allowing us to use his microwave simulation results. The authors would like to thank the following in supplying some of the radar data used in the investigation: M. MacDonald, NOAA/NWS (RADAP-II), and E. Barrett and C. Kidd, University of Bristol (FRONTIERS). Additionally, the authors would like to thank R. Savage and A. Koscielny of Hughes Aircraft Company for supplying the documentation of the synthetic 85V algorithm. Finally, the authors are thankful for the manuscript comments supplied by our colleagues F. Weng (Caelum Research Corp.), J. Alishouse (NOAA), and D. Tarpley (NOAA). This work was supported through the NOAA Climate and Global Change Program.

TABLE A2. Coefficients for $TA85_{vs}$ calculations.

Category	Constant	TA_{19V}	TA_{19H}	TA_{22V}	TA_{37V}	TA_{37H}	TA_{85H}
1	67.4105	0.343107	−0.166661	0.064316	0.299581	−0.328124	0.517033
2	77.5119	−0.571147	0.311122	0.201946	1.014484	−0.748197	0.462336
3	45.7987	0.418078	−0.041601	−0.119912	0.298003	−0.420198	0.702025
4	21.3573	−0.207214	0.189461	−0.073309	0.855635	−0.654701	0.813340
5	15.8786	−0.177043	0.085521	0.113283	0.567277	−0.489962	0.849420
6	23.9710	−0.356680	0.266729	−0.083909	0.883401	−0.711874	0.919301
7	42.0507	0.0	0.0	−0.347921	0.437676	−0.209622	0.988095

TABLE A3. Comparison of actual vs synthetic TA85V for RADAP-II and SSM/I matchups.

	No. of obs.		TA_{85V} mean (K)		TA_{85VS} mean (K)		rms (K)	
Category	Land	Ocean	Land	Ocean	Land	Ocean	Land	Ocean
1	0	647	—	266.0	—	266.6	—	2.1
2	0	0	—	—	—	—	—	—
3	0	61	—	258.7	—	258.1	—	3.8
4	3245	83	268.5	241.0	269.1	242.1	1.7	2.6
5	0	0	—	—	—	—	—	—
5	522	8	244.9	218.8	244.7	218.9	2.0	2.6
7	458	0	213.4	—	214.3	—	2.6	—

APPENDIX

Synthetic 85V Algorithm and Error Statistics

The first SSM/I instrument was launched in June 1987. Due to variations in the sun angle, the instrument is subjected to a large range in solar heating (Hollinger 1991). During late 1987, the heating of the instrument began approaching the maximum safe limit of operation and on 2 December 1987 the SSM/I was turned off to avoid potential damage to the instrument. On 12 January 1988, the instrument was turned back on after the heating problem began to subside. At this time, all channels except the 85V began to perform at levels prior to the December turn off. As time progressed, the noise on the 85V continued to worsen, so that by approximately January 1989, the 85V channel became unusable. Actually, noise levels by May 1988 increased to make routine use of the data difficult. Since many of the original algorithms developed by the Cal/Val team relied on the 85V channel, the Hughes Aircraft Company (R. Savage and A. J. Koscielny) was tasked by the U.S. Air Force to develop an algorithm to "synthesize" the 85V antenna temperature (hereafter denote TA_{85VS}) using combinations of the remaining six channels. Since there is strong correlations among the various channels, this was not seen as a very difficult task. The only documented information regarding the algorithm is provided in a Hughes document written by A. Kqscielny graciously provided to the authors by R. Savage. Some of the information is summarized below. It should be noted that since this method was developed for "antenna temperatures" and not "brightness temperatures," one needs to be able to convert from TB to TA, then back to TB when using this procedure. The simplest way to do this is by using the methodology presented by Wentz (1991).

The TA_{85VS} algorithm was developed as follows. A training dataset consisting of TA measurements from various time periods in 1987 over various surface features was assembled and subjected to a series of statistical analyses. There were 14 different surface types analyzed. The TA_{85V} was then subjected to a stepwise linear regression analysis for the entire dataset, as well as the data for each surface separately. The best results were found when the data were stratified into seven different surface categories (see Table A1) and when all of the channels were used. Root-mean-square errors ranged from as low as 1.6–3.4 K. The regression coefficients to be applied for each of the categories j is presented in Table A2, and take the form

$$TA^{j}_{85V} = a^{j} + \sum_{i=1,6} b^{j} TA^{i,j},$$

where $i = 1, 6$ and represents SSM/I channels 19V, 19H, 22V, 37V, 37H, and 85H and a^j and b^j are the coefficients.

To independently validate the performance of the algorithm under raining conditions, we examined data from 1987, which was a period where the 85V channel was functioning properly. The SSM/I–RADAP-II matchup dataset was used to generate the original and synthesized measurements. Comparisons between the TA_{85V} and the TA_{85VS} were made and are summarized in Table A3. As can be seen, rms errors comparable to those given in Table A1 were found. In addition, relatively small biases were found in our analysis.

REFERENCES

Adler, R. F., and I. M. Hakkarinen, 1991: Aircraft multifrequency passive microwave observations of light precipitation over the ocean. *J. Atmos. Oceanic Technol.*, **8**, 201–220.

——, H. Y. M. Yeh, N. Prasad, W. K. Tao, and J. Simpson, 1991: Microwave simulations of a tropical rainfall system with a three-dimensional cloud model. *J. Appl. Meteor.*, **30**, 924–953.

Alishouse, J. C., R. R. Ferraro, and J. V. Fiore, 1990: Inference of oceanic rainfall properties from the Nimbus 7 SMMR. *J. Appl. Meteor.*, **29**, 551–560.

Austin, P. M., 1987: Relation between measured radar reflectivity and surface rainfall. *Mon. Wea. Rev.*, **115**, 1053–1070.

Bauer, P., and P. Schluessel, 1993: Rainfall, total water, ice water, and water vapor over sea from polarized microwave simulations and Special Sensor Microwave/Imager data, *J. Geophys. Res.*, **98**, 20 737–20 759.

Berg, W., and R. Chase, 1992: Determination of mean rainfall from the Special Sensor Microwave/Imager (SSM/I) using a mixed lognormal distribution. *J. Atmos. Oceanic Technol.*, **9**, 129–141.

Dodge, J. C., and H. M. Goodman, 1994: The WetNet Project. *Remote Sens. Rev.*, **11**, 5–211.

Ferraro, R. R., N. C. Grody, J. C. Alishouse, and G. Marks, 1992: The calibration of an SSM/I scattering index for rain rate retrievals using RADAP-II and AMeDAS radar data. *Proc. Sixth*

Conf. on Satellite Meteorology and Oceanography, Atlanta, GA, Amer. Meteor. Soc., 290–295.

——, N. C. Grody, and G. F. Marks, 1994: Effects of surface conditions on rain identification using the SSM/I. *Remote Sens. Rev.*, **11**, 195–210.

Greene, D. R., J. D. Nilsen, R. E. Saffle, D. W. Holmes, M. D. Hudlow, and P. R. Anhert, 1983: RADAP-II, an interim radar data processor. *Proc. 21st Conf. on Radar Meteorology*, Edmonton, Alberta, Canada, Amer. Meteor. Soc., 404–408.

Grody, N. C., 1991: Classification of snow cover and precipitation using the Special Sensor Microwave/Imager (SSM/I). *J. Geophys. Res.*, **96**, 7423–7435.

——, and R. R. Ferraro, 1992: A comparison of passive microwave retrieval methods. *Proc. Sixth Conf. on Satellite Meteorology and Oceanography*, Atlanta, GA, Amer. Meteor. Soc., 60–65.

Hakkarinen, I. M., and R. F. Adler, 1988: Observations of precipitating convective systems at 92 and 183 GHz: Aircraft results. *Meteor. Atmos. Phys.*, **38**, 164–182.

Hinton, B. B., W. S. Olson, D. W. Martin, and B. Auvine, 1992: A passive microwave algorithm for tropical oceanic rainfall. *J. Appl. Meteor.*, **31**, 1379–1395.

Hollinger, J., 1991: DMSP SSM/I calibration/validation. Final Report parts I & II, Naval Research Laboratory, Washington, DC, 453 pp.

——, R. Lo, G. Poe, R. Savage, and J. Pierce, 1987: *Special Sensor Microwave Imager User's Guide.* Naval Research Laboratory, 120 pp.

Joss, J., and A. Waldvogel, 1990: Precipitation measurement and hydrology. *Radar in Meteorology.* D. Atlas, Ed., American Meteorological Society, 577–606.

Kummerow, C., and J. A. Weinman, 1988: Determining microwave brightness temperatures from precipitating horizontally finite and vertically structured clouds. *J. Geophys. Res.*, **93**, 3720–3728.

Petty, G. W., 1990: On the response of the Special Sensor Microwave/Imager to the marine environment—Implications for geophysical parameter retrievals. Ph.D. dissertation, University of Washington, 291 pp. [Available from University Microfilms International, Ann Arbor, MI 48106.]

——, and K. B. Katsaros, 1990: Precipitation observed over the South China Sea by the *Nimbus-7* Scanning Multichannel Microwave Radiometer during winter MONEX. *J. Appl. Meteor.*, **29**, 273–287.

——, and ——, 1992: *Nimbus-7* SMMR precipitation observations calibrated against surface radar during TAMEX. *J. Appl. Meteor.*, **31**, 489–505.

Prabhakara, C., G. Dalu, G. L. Liberti, J. J. Nucciarone, and R. Suhasini, 1992: Rainfall estimation over oceans from SMMR and SSM/I microwave data. *J. Appl. Meteor.*, **31**, 532–552.

Spencer, R. W., 1986: A satellite passive 37 GHz scattering-based method for measuring oceanic rain rates. *J. Climate Appl. Meteor.*, **25**, 754–766.

——, H. M. Goodman, and R. E. Hood, 1989: Precipitation retrieval over land and ocean with the SSM/I, Part I: Identification and characteristics of the scattering signal. *J. Atmos. Oceanic Technol.*, **6**, 254–273.

Weng, F., 1992: Vector radiative transfer model: Application to rainfall retrieval with microwave radiometric data. Ph.D. dissertation, Colorado State University, 192 pp.

——, and N. C. Grody, 1994: Retrieval of cloud liquid water using the Special Sensor Microwave Imager (SSM/I) data. *J. Geophys. Res.*, **99**, 25 535–25 551.

Wentz, F. J., 1990: West Coast storm forecasting with SSM/I. Vol. I: Final Tech. Report, Remote Sensing Systems, Santa Rosa, CA, 42 pp.

——, 1991: *User's Manual—SSM/I Antenna Temperature Tapes* (Revision 1). Remote Sensing Systems, 70 pp.

Wilheit, T. T., A. T. C. Chang, M. S. V. Rao, E. B. Rodgers, and J. S. Theon, 1977: A satellite technique for quantitatively mapping rainfall rates over the oceans. *J. Appl. Meteor.*, **16**, 551–560.

——, ——, and L. S. Chiu, 1991: Retrieval of monthly rainfall indices from microwave radiometric measurements using probability distribution functions. *J. Atmos. Oceanic Technol.*, **8**, 118–136.

Wu, R., and J. A. Weinman, 1984: Microwave radiances from precipitation clouds containing aspherical ice, combined phase, and liquid hydrometeors. *J. Geophys. Res.*, **89**, 7170–7178.